Title
Quasar-Lyman α forest cross-correlation from BOSS DR11: Baryon Acoustic Oscillations

Journal
Journal of Cosmology and Astroparticle Physics, 2014(05)

ISSN
1475-7516

Authors
Font-Ribera, Andreu
Kirkby, David
Busca, Nicolas
et al.

Publication Date
2014-05-01

DOI
10.1088/1475-7516/2014/05/027

Prepared for submission to JCAP

Quasar-Lyman α Forest Cross-Correlation from BOSS DR11 : Baryon Acoustic Oscillations

Andreu Font-Ribera,[a,b] **David Kirkby,**[c] **Nicolas Busca,**[d] **Jordi Miralda-Escudé,**[e,f] **Nicholas P. Ross,**[b,g] **Anže Slosar,**[h] **James Rich,**[i] **Éric Aubourg,**[d] **Stephen Bailey,**[b] **Vaishali Bhardwaj,**[j,b] **Julian Bautista,**[d] **Florian Beutler,**[b] **Dmitry Bizyaev,**[i] **Michael Blomqvist,**[c] **Howard Brewington,**[k] **Jon Brinkmann,**[k] **Joel R. Brownstein,**[l] **Bill Carithers,**[b] **Kyle S. Dawson,**[l] **Timothée Delubac,**[i] **Garrett Ebelke,**[k] **Daniel J. Eisenstein,**[m] **Jian Ge,**[n] **Karen Kinemuchi,**[j] **Khee-Gan Lee,**[o] **Viktor Malanushenko,**[k] **Elena Malanushenko,**[k] **Moses Marchante,**[j] **Daniel Margala,**[c] **Demitri Muna,**[p] **Adam D. Myers,**[q] **Pasquier Noterdaeme,**[r] **Daniel Oravetz,**[j] **Nathalie Palanque-Delabrouille,**[i] **Isabelle Pâris,**[s] **Patrick Petitjean,**[r] **Matthew M. Pieri,**[t] **Graziano Rossi,**[i] **Donald P. Schneider,**[u,v] **Audrey Simmons,**[j] **Matteo Viel,**[w,x] **Christophe Yeche,**[i] **Donald G. York**[y]

[a]Institute of Theoretical Physics, University of Zurich, Winterthurerstrasse 190, 8057 Zurich, Switzerland

[b]Lawrence Berkeley National Laboratory, 1 Cyclotron Road, Berkeley, CA, USA

[c]Department of Physics and Astronomy, University of California, Irvine, CA 92697, USA

[d]APC, Université Paris Diderot-Paris 7, CNRS/IN2P3, CEA, Observatoire de Paris, 10, rue A. Domon & L. Duquet, Paris, France

[e]Institut de Ciències del Cosmos (IEEC/UB), Martí i Franquès 1, 08028 Barcelona, Catalonia

[f]Institució Catalana de Recerca i Estudis Avançats, Passeig Llus Companys 23, 08010 Barcelona, Catalonia

[g]Department of Physics, Drexel University, 3141 Chestnut Street, Philadelphia, PA 19104, USA

[h]Brookhaven National Laboratory, Blgd 510, Upton NY 11375, USA

[i]CEA, Centre de Saclay, IRFU, 91191 Gif-sur-Yvette, France

[j]Department of Astronomy, University of Washington, Box 351580, Seattle, WA 98195, USA

[k]Apache Point Observatory and New Mexico State University, P.O. Box 59, Sunspot, NM, 88349-0059, USA
[l]Department of Physics and Astronomy, University of Utah, 115 S 1400 E, Salt Lake City, UT 84112, USA
[m]Harvard-Smithsonian Center for Astrophysics, 60 Garden Street, Cambridge, MA 02138, USA
[n]Astronomy Department, University of Florida, 211 Bryant Space Science Center, Gainesville, FL 32611-2055, USA
[o]Max-Planck-Institut für Astronomie, Königstuhl 17, D-69117 Heidelberg, Germany
[p]Department of Astronomy, Ohio State University, Columbus, OH, 43210, USA
[q]Department of Physics and Astronomy 3905, University of Wyoming, 1000 East University, Laramie, WY 82071, USA
[r]Institut d'Astrophysique de Paris, CNRS-UPMC, UMR7095, 98bis bd Arago, 75014 Paris, France
[s]Departamento de Astronomía, Universidad de Chile, Casilla 36-D, Santiago, Chile
[t]Institute of Cosmology and Gravitation, Dennis Sciama Building, University of Portsmouth, Portsmouth, PO1 3FX, UK
[u]Department of Astronomy and Astrophysics, The Pennsylvania State University, University Park, PA 16802
[v]Institute for Gravitation and the Cosmos, The Pennsylvania State University, University Park, PA 16802
[w]INAF, Osservatorio Astronomico di Trieste, Via G. B. Tiepolo 11, 34131 Trieste, Italy
[x]INFN/National Institute for Nuclear Physics, Via Valerio 2, I-34127 Trieste, Italy
[y]Deptartment of Astronomy and Astrophysics and The Fermi Institute, The University of Chicago, 5640 South Ellis Avenue, Chicago, IL 60615, USA

E-mail: afont@lbl.gov

Abstract. We measure the large-scale cross-correlation of quasars with the Lyα forest absorption, using over 164,000 quasars from Data Release 11 of the SDSS-III Baryon Oscillation Spectroscopic Survey. We extend the previous study of roughly 60,000 quasars from Data Release 9 to larger separations, allowing a measurement of the Baryonic Acoustic Oscillation (BAO) scale along the line of sight $c/(H(z=2.36)\,r_s) = 9.0 \pm 0.3$ and across the line of sight $D_A(z=2.36)\,/\,r_s = 10.8 \pm 0.4$, consistent with CMB and other BAO data. Using the best fit value of the sound horizon from Planck data ($r_s = 147.49\,\mathrm{Mpc}$), we can translate these results to a measurement of the Hubble parameter of $H(z=2.36) = 226 \pm 8\,\mathrm{km\,s^{-1}\,Mpc^{-1}}$ and of the angular diameter distance of $D_A(z=2.36) = 1590 \pm 60\,\mathrm{Mpc}$. The measured cross-correlation function and an update of the code to fit the BAO scale (baofit) are made publicly available.

Keywords: large-scale structure: redshift surveys — large-scale structure: Lyman alpha forest — cosmology: dark energy

Contents

1 Introduction

Fifteen years ago, two independent studies of the luminosity distance of type Ia supernovae ([1],[2]) showed that the Universe was undergoing an accelerated expansion. In order to explain such an unintuitive result, different authors have suggested the need for a cosmological constant in Einstein's equations of general relativity, more profound modifications of the gravitational theory, or the presence of a new energy component usually referred to as *dark energy*.

Following this discovery, different cosmological probes have provided a wealth of new data, allowing us to constrain the cosmological parameters of the model at a few-percent level. The simplest possible solution, a flat universe with a cosmological constant, is able to explain all current data [3], and ongoing and future cosmological surveys will continue to reduce the errorbars of these measurements and place even more stringent constraints on the models.

There are different observational probes that can measure the history of the accelerated expansion (see [4] for a review). One is the measurement of the Baryon Acoustic Oscillation (BAO) scale on the clustering of any tracer of the density field, which can be used as a cosmic ruler to study the geometry of the Universe [5]. This technique has gained considerable attention during the last decade, and the list of BAO measurements is rapidly increasing.

In theory, any tracer of the large-scale matter distribution can be used to measure BAO. Even though the first measurements came from the clustering of low redshift galaxies (Sloan Digital Sky Survey [6] at $0.2 < z < 0.4$, Two-degree-Field Galaxy Redshift Survey [7] at $0.1 < z < 0.2$), and the tightest constraints are obtained from intermediate redshift galaxy surveys (WiggleZ Dark Enery Survey [8] at $0.4 < z < 0.8$, Baryon Oscillation Spectroscopic Survey [9] at $0.4 < z < 0.7$), there are also a variety of undergoing or planned surveys that aim to measure BAO at higher redshift from the clustering of x-ray sources (eROSITA [10]), 21cm emission (Canadian Hydrogen Intensity Mapping Experiment [1], Baryon Acoustic Oscillation Broadband and Broad-beam Array [11]), Lyα emitting galaxies (Hobby-Eberly Telescope Dark Energy Experiment [12], Dark Energy Spectroscopic Instrument [13]) and quasars (Extended Baryon Oscillation Spectroscopic Survey [14]).

The spatial distribution of neutral hydrogen, as traced by the Lyman-α forest (Lyα forest) can also be used to measure BAO. The first measurement of the three-dimensional large-scale structure of Lyα absorption was presented in [15], using over 14,000 spectra from the first year of BOSS. This study was extended using approximately 50,000 quasar spectra from the ninth data release of SDSS (DR9, [16]), and the first detections of the BAO at $z = 2.4$ were presented in [17], [18] and [19].

Using the same set of spectra, [20] presented an analysis of the large scale cross-correlation of quasars and the Lyα absorption. In this analysis the cross-correlation was

[1] http://chime.phas.ubc.ca/

clearly detected up to separations of $r \sim 70\,h^{-1}\,$Mpc, and was accurately described by a linear bias and redshift-space distortion theory for comoving separations $r > 15\,h^{-1}\,$Mpc. Their measurement of the quasar bias of $b_q = 3.64 \pm 0.14$ was fully consistent with measurements of the quasar auto-correlation function at the same redshift, e.g., [21].

In this paper, we use over 164,000 quasars from the eleventh data release of SDSS (DR11, which will be publicly released at the end of 2014 together with DR12) to extend the measurement of the cross-correlation to larger separations, and we present an accurate determination of the BAO scale in cross-correlation at high-redshift ($z \sim 2.4$).

Throughout, we use the fiducial cosmology ($\Omega_m = 0.27$, $\omega_b = 0.0227$, $h = 0.7$, $\sigma_8 = 0.8$, $n_s = 0.97$) that was used in the previous Lyα BAO measurements ([17], [18], [19]). We use the publicly available code CAMB [22] to compute the comoving distance to the sound horizon at the redshift at which baryon-drag optical depth equals unity, $z_{drag} = 1059.97$, and obtain a value of $r_s = 149.72\,$Mpc. Some previous BAO studies have used the equations from [23] to compute the value of r_s, resulting in a few percent difference with respect to the value computed with CAMB, as discussed in [3].

We start by introducing our data sample in section 2. In section 3 we present our measurement of the quasar-Lyα cross-correlation and summarize our analysis method. In section 4 we describe our fits of the BAO scale, present our main results, and test possible systematic effects. In section 5 we compare our results with previous BAO measurements at similar redshifts.

2 Data Sample

In this section we describe the data set used in this study, and present a series of references for further details.

The eleventh Data Release (DR11) of the SDSS-III Collaboration ([24], [25], [26], [27], [28], [29]) contains all spectra obtained during the first four years of the Baryon Oscillation Spectroscopic Survey (BOSS, [30]), including spectra of 238,978 visually confirmed quasars. The quasar target selection used in BOSS is summarized in [31], and combines different targeting methods described in [32], [33], and [34].

In this study we measure the cross-correlation of two tracers of the underlying density field: the number density of quasars and the Lyα absorption along a set of lines of sight. We will use the term "quasar sample" to refer to the quasars used as tracers of the density field, and the term "Lyα sample" to refer to those quasar lines of sight where the Lyα absorption is measured.

2.1 Quasar sample

We use a preliminary version of the DR11Q quasar catalog, an updated version of the DR9Q catalog presented in [35]. This catalog contains a total of 238,978 visually confirmed quasars, distributed in an area of 8976 square degrees in two disconnected parts of the sky: the South Galactic Cap (SGC) and the North Galactic Cap (NGC). To avoid repeated observations of the same object, we only use quasars in the catalog that have the SPECPRIMARY flag [30].

The performance of the BOSS spectrograph rapidly deteriorates at wavelengths bluer than $\lambda \sim 3650\,\text{Å}$, corresponding to a Ly$\alpha$ absorption of $z = 2$; this wavelength sets the lower limit in the redshift range used in this study. Since the number of identified quasars drops rapidly at high redshift, we restrict our quasar sample to those with redshifts in the range $2.0 \leq z_q \leq 3.5$. This redshift constraint reduces the number of quasars used as tracers of the density field to 164,017. In this paper we use the Z_VI redshift estimate from [35].

2.2 Lyα sample

Not all spectra from the quasar sample are included in our Lyα sample. We first drop the spectra from quasars with a redshift lower than $z_q = 2.15$, since only a small part of their Lyα forest can be observed with the BOSS spectrograph. This choice reduces the number of spectra to 153,496.

During the visual inspection, Broad Absorption Line quasars (BAL) are identified [35]. We discard any spectra from BAL quasars, reducing the number of spectra to 136,431. We finally exclude spectra with less than 150 pixels covering the Lyα forest, further reducing the number of spectra used in the Lyα sample to 130,825. We use the same definition of the Lyα forest as in [36], which contains all pixels in the rest-frame wavelength range $1040\,\text{Å} \leq \lambda_{\text{rest}} \leq 1200\,\text{Å}$.

In the left panel of figure 1 we show the redshift distribution of objects in the quasar sample (red in the NGC, blue in the SGC) and the distribution of these quasars that have spectra included in the Lyα sample (green in the NGC, purple in the SGC).

We use an updated (DR11) version of the Damped Lyman α system (DLA) catalogue from [37], based on DLA profile recognition as described in [38], to mask the central part of DLA in the spectra (up to a transmitted flux fraction of $F < 0.8$), and correct the rest of the spectra using the inferred Voigt profile.

We correct the noise estimate from the pipeline using the method described in [17]. Following the same reference, we rebin our spectra by averaging the flux over three adjacent pipeline pixels. These new pixels have a width of $210\,\text{km}\,\text{s}^{-1}$, $\sim 2\ h^{-1}\,\text{Mpc}$ at the redshift of interest, much smaller than the minimum separation in which we are interested ($r > 40\,h^{-1}\,\text{Mpc}$), and smaller than the width of the BAO peak ($\Delta r \sim 25\,h^{-1}\,\text{Mpc}$). We will use the term "pixel" to refer to these rebinned pixels.

2.3 Independent sub-samples

In section 3 we explain the method to estimate the covariance matrix of our measurement. To reduce the required computing time, the survey is split into 66 sub-samples with a similar number of quasars and combine the measurement of each sub-sample assuming that they are independent. The right panel of figure 1 shows the different sub-samples, 51 of them in the north galactic cap (NGC) and 15 in the south (SGC).

These sub-samples are also used in section 4 to compute bootstrap errors on the best fit parameters. Since we are interested in scales smaller than $150\,h^{-1}\,\text{Mpc}$ and the typical area of these sub-samples is roughly $(800\,h^{-1}\,\text{Mpc})^2$ ($140\,\text{deg}^2$ at $z = 2.4$), the assumption that the sub-samples are independent is justified.

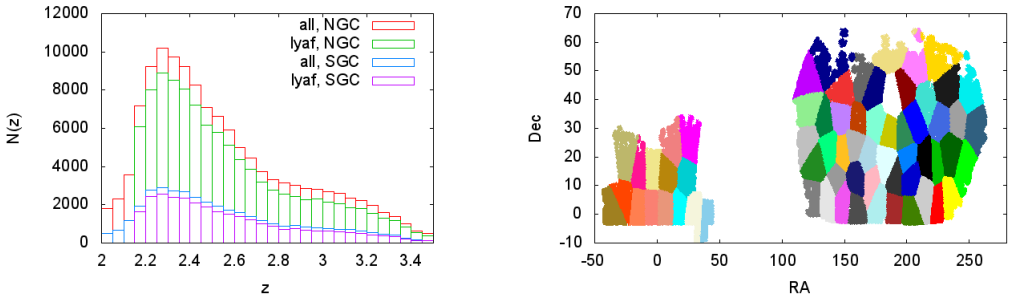

Figure 1: Left panel: Redshift distribution of the 164,017 quasars used as density tracers (red in NGC, blue in SGC), and of the 130,825 quasars with Lyα spectra (green in NGC, purple in SGC). Right panel: DR11 footprint in J2000 equatorial coordinates with the 66 sub-samples indicated in different colors.

3 Cross-correlation

In this section we briefly describe the method used to measure the cross-correlation and its covariance matrix, referring the reader to previous publications for a detailed explanation ([39], [20]), and present the measured cross-correlation.

3.1 Continuum fitting

The first step necessary to estimate the Lya transmitted flux fraction $F(\lambda) = e^{-\tau(\lambda)}$ from a set of pixels with flux $f(\lambda)$ is estimating the quasar continuum, $C_q(\lambda)$,

$$F(\lambda) = \frac{f(\lambda)}{C_q(\lambda)} \ . \tag{3.1}$$

Among various approaches for the determination of the continuum available in the literature, we use *Method 2* in [17], which is also being used for the analysis of the BAO Lya autocorrelation for DR11 [36]. This method assumes that all quasars have the same continuum $\bar{C}(\lambda_{\rm rest})$, except for a linear multiplicative function that varies for each quasar:

$$C_q(\lambda) = (a_q + b_q\lambda)\bar{C}(\lambda_{\rm rest}) \ , \tag{3.2}$$

where a_q and b_q are fitted to match an assumed probability distribution function (PDF), as explained in [17].

The construction of the continuum is a critical step for those Lyα studies focused on the line of sight power spectrum or in the flux PDF, where errors in the continuum fitting can systematically bias the results. In three dimensional clustering measurements of Lyα absorption, one would expect that the continuum fitting errors in different lines of sight are uncorrelated, getting rid of any potential bias in the measurement. However, as noted by [15], if the continuum of each quasar is rescaled in order to match an external mean transmission

or flux PDF, the errors in the continuum fitting will be correlated with large scale density fluctuations. We discuss this issue further in section 3.4.

In section 4 (table 1) we present an alternative analysis using a different method to fit the continua, based on the Principal Component Analysis (PCA) presented in [40], and show that the measurement of the BAO scale is in very good agreement with our fiducial analysis.

3.2 From flux to δ_F

Using the continua described above, we now measure the mean transmitted flux fraction $\bar{F}(z)$, also known as the "mean transmission". The redshift of absorption z is related to the observed wavelength λ by the Lyα transition line $\lambda_\alpha = 1216\,\text{Å} = \lambda/(1+z)$. We measure the mean transmission as a function of redshift, in $N_z = 300$ bins between $1.9 \leq z \leq 3.4$,

$$\bar{F}(z) = \left\langle \frac{f(\lambda)}{C_q(\lambda)} \right\rangle \ , \tag{3.3}$$

where the average is computed over all pixels in each redshift bin. The Lyα absorption fluctuation is then defined as

$$\delta_F = \frac{f}{C_q \bar{F}} - 1 \ . \tag{3.4}$$

As noted in [17], there are sharp features in the measurement of the mean transmission due to imperfections in the calibration vector of the BOSS data reduction pipeline. We do not expect this error to bias our results on the quasar-Lyα cross-correlation because it should be corrected when the quasar spectra are divided by the measured mean transmission, and any residual errors are not expected to correlate with the quasar detection efficiency that varies across the BOSS survey area.

3.3 Estimator and covariance matrix

We estimate the cross-correlation ξ_A between quasars and Lyα absorption, in a bin r_A, employing the same method that was used in previous analyses of cross-correlations in BOSS ([39], [20]):

$$\hat{\xi}_A = \frac{\sum_{i \in A} w_i \, \delta_{Fi}}{\sum_{i \in A} w_i} \ , \tag{3.5}$$

where the sum is over all pixels i that are at a separation r_i in bin A from a quasar, and where the weights w_i are computed independently at each pixel from the pipeline noise variance and assuming a model for the intrinsic Lyα absorption variance (equation 3.10 in [39]).

The covariance matrix of the correlation measurements in two bins A and B, $\tilde{C}_{AB}$, is too large to be computed using resampling techniques or from synthetic data sets. Instead we use an analytical estimate similar to the method used in Lyα auto-correlation analyses ([15],[36]), which was first applied to cross-correlations studies in [39] :

$$\tilde{C}_{AB} \equiv \left\langle \hat{\xi}_A \hat{\xi}_B \right\rangle - \left\langle \hat{\xi}_A \right\rangle \left\langle \hat{\xi}_B \right\rangle = \frac{\sum_{i \in A} \sum_{j \in B} w_i \ w_j \ C^F_{ij}}{\sum_{i \in A} w_i \ \sum_{j \in B} w_j} \ , \tag{3.6}$$

where $C_{ij}^F = \langle \delta_{Fi} \delta_{Fj} \rangle$ is the correlation of the Lyman alpha fluctuations δ_F measured in pixels i and j, separated in redshift space by $\mathbf{r}_{ij}$, and includes both the cosmological signal and the contribution from instrumental noise when $i = j$. In this study, we further simplify the calculation by ignoring the correlation among Lyα pixels in different lines of sight.

This method assumes Gaussian errors and ignores the contribution from cosmic variance, a reasonable approximation given the large volume of the survey and its sparse sampling. We also assume that the variance in the quasar density field is dominated by shot noise, which is justified on the same grounds. It is useful to examine these assumptions in Fourier space (see appendix B for an extended discussion on this). The variance in the measurement of the cross-power spectrum $P_{qF}(\mathbf{k})$ for a single Fourier mode $\mathbf{k}$ can be approximated by :

$$var\left(P_{qF}(\mathbf{k})\right) = P_{qF}(\mathbf{k})^2 + \left(P_{qq}(\mathbf{k}) + n_q^{-1}\right)\left(P_{FF}(\mathbf{k}) + P^{1D}(k\mu)\, n_{eff}^{-1}\right) \ , \tag{3.7}$$

where n_q is the quasar density, P_{qq} the quasar auto-power spectrum, P_{FF} the Lyα auto-power spectrum, P^{1D} the line of sight Lyα power spectrum and n_{eff} the effective density of Lyα lines of sight as defined in [41]. Ignoring cosmic variance is equivalent to removing the term P_{qF}^2, while assuming that quasars are shot-noise dominated is equivalent to removing the P_{qq} term. These approximations are supported by the analysis of the various terms in this equation presented in B.

We use 16 bins of constant width $10\,h^{-1}\,$Mpc in transverse separation $r_\perp$, up to a maximum separation of $r_\perp < 160\,h^{-1}\,$Mpc. Since $r_\parallel$ can be positive (pixel behind the quasar) or negative (pixel in front of the quasar) we use 32 bins in $r_\parallel$ with the limits $-160\,h^{-1}\,\text{Mpc} < r_\parallel < 160\,h^{-1}\,$Mpc. We use a single bin in redshift, ranging from $2.0 < z < 3.4$. Other BAO studies that measure the correlation in multipoles, or grids defined in the ($r = \sqrt{r_\parallel^2 + r_\perp^2}$, $\mu = r_\parallel / r$) plane, use narrower bins in order to better resolve the BAO peak. Coarser bins can be used in studies where the correlation is measured in the ($r_\parallel$,$r_\perp$) plane, since each point corresponds to a different value of r. For instance, we cover 48 different values of r in the range $90\,h^{-1}\,\text{Mpc} < r < 120\,h^{-1}\,$Mpc.

As discussed in **??**, the cross-correlations and their covariance matrices are measured in 66 sub-samples (shown in figure 1), $\hat{\xi}_\alpha$ and $\tilde{C}_\alpha$. Assuming that these are independent, the optimal way to combine them is:

$$\tilde{C}^{-1} = \sum_\alpha \tilde{C}_\alpha^{-1} \ , \qquad \hat{\xi} = \tilde{C} \sum_\alpha \tilde{C}_\alpha^{-1} \hat{\xi}_\alpha \ . \tag{3.8}$$

When measuring the correlation in one of the sub-samples we only use Lyα pixels from spectra in that given part of the sky. However, we cross-correlate the absorption in these pixels not only with quasars from the sub-sample, but also with quasars in the neighboring sub-samples. We are therefore not losing any interesting quasar-pixel pairs, at the expense of adding a small correlation between the different measurements.

3.4 Measured cross-correlation

The quasar-Lyα cross-correlation that is obtained with the method just described is plotted in the left panel of figure 2. The model that we use to fit its functional form has two

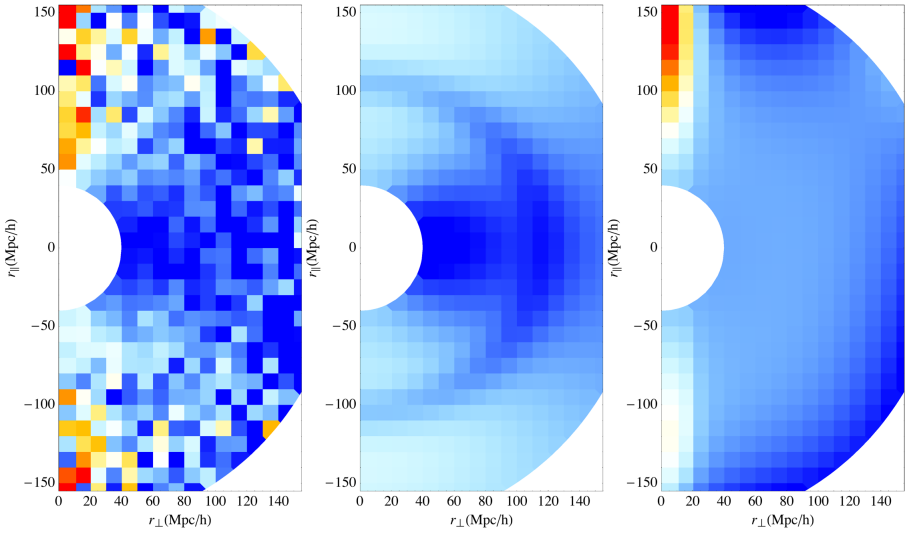

Figure 2: Left panel: Observed quasar-Lyα cross-correlation, $r^2\xi(r_\parallel, r_\perp)$, as a function of line of sight ($r_\parallel$) and transverse ($r_\perp$) separations. Mid panel: Cosmological contribution to the best fit model (see next section). Right panel: contribution of the broadband distortion to the best fit model. The fit to the observed cross-correlation is the sum of the middle and right panels. As discussed in the text, the asymetric nature of the broadband distortion can be explained by the continuum fitting method.

components: first, the theoretical cross-correlation function in the absence of systematics, and second, a broadband function that models systematic distortions that are introduced into the measurement. This will be described in detail in section 4, but it is useful to discuss now the general reason to fit a model with these two terms.

The middle panel in figure 2 shows the cosmological component of the best fit model, and the right panel is the broadband distortion part. The fit to the observed cross-correlation is the sum of the functions in the middle and right panels. The shape of the broadband distortion and its asymetric nature can be explained by our method to determine the quasar continuum, which involves fitting a multiplicative function $a_q + b_q\lambda$ to each spectrum to match an assumed PDF of the transmission F. This effectively removes large-scale power in the observed Lyα forest: roughly speaking, the mean value and the gradient of the large-scale density fluctuations over the line of sight of each Lyα spectrum are removed by the continuum fitting operation.

The distortion effect that this introduces on three-dimensional correlation measurements was first discussed in the context of the Lyα auto-correlation in Appendix A of [15]. The corresponding distortion on the cross-correlation was considered in [39], where it was modeled and computed in terms of the quasar redshift distribution and the interval of the observed Lyα forest spectra. This expected distortion, plotted in figure 17 of [39], is a strong function of $r_\perp$ and a weaker function of $r_\parallel$, and is asymetric under a sign change of $r_\parallel$ because the average quasar redshift is higher than the average Lyα pixel redshift.

An analytical prescription to correct for this distortion in the fitted theoretical model was presented in [39], valid for the simpler continuum fitting method that was used there. This was crucial for that work and in [20], where the goal was to accurately measure the full shape of the cross-correlation to obtain the bias and redshift distortion parameters.

In this paper, our goal is to measure the position of the BAO peak without any dependence on possible systematics in our modeling of the broadband shape of the cross-correlation. We therefore decide not to apply any correction to the theoretical model. Instead, a broadband term is added to the cross-correlation with enough free parameters to absorb a generic smooth distortion, as explained in section 4. This approach, also used in the recent BAO measurements from the Lyα auto-correlation ([17], [18], [19]), relies on the narrowness of the BAO peak, which decouples its position from the broadband shape. Unfortunately, this degrades our ability to measure the bias and redshift distortion parameters because they are affected by the broadband model.

4 Fitting the BAO Scale

In this section we describe the method used to measure the scale of the Baryon Acoustic Oscillations (BAO) from the measured cross-correlations, and present our main results. We conclude with a detailed analysis of possible sources of systematic errors.

4.1 BAO model

We adapted the publicly available fitting code baofit [19] to work with cross-correlations. The code can be downloaded from the URL in footnote [2], together with the measured cross-correlation and its covariance matrix, as described in appendix A.

A detailed description of the fitting code can be found in [19]; here we only summarize the main points and highlight the differences between fitting the Lyα auto-correlation and the quasar-Lyα cross-correlation.

We model the measured cross-correlation $\xi(r_\parallel, r_\perp)$ as a sum of the *cosmological* correlation $\xi_{\rm cosmo}$ and a broadband distortion term $\xi_{\rm bb}$ due primarily to continuum fitting (as discussed in section 3.4)

$$\xi(r_\parallel, r_\perp) = \xi_{\rm cosmo}(r_\parallel, r_\perp, \alpha_\parallel, \alpha_\perp) + \xi_{\rm bb}(r_\parallel, r_\perp) \ . \tag{4.1}$$

The quantity $\xi_{\rm cosmo}$ is described as a sum of two terms

$$\xi_{\rm cosmo}(r_\parallel, r_\perp) = \xi_{\rm smooth}(r_\parallel, r_\perp) + a_{\rm peak} \cdot \xi_{\rm peak}(r_\parallel \alpha_\parallel, r_\perp \alpha_\perp) \ , \tag{4.2}$$

where $a_{\rm peak}$ controls the amplitude of the BAO peak. The correct $\xi_{\rm cosmo}$ in the Cold Dark Matter standard model is obtained only for $a_{\rm peak} = 1$, which we use in all of our analyses except when we want to test the consistency of our results with the prediction for the peak amplitude (row labeled AMP in table 1).

[2] http://darkmatter.ps.uci.edu/baofit/

The main goal of this study is to measure the scale of BAO relative to the fiducial cosmological model, along the line of sight $\alpha_{\parallel}$ and across the line of sight $\alpha_{\perp}$:

$$\alpha_{\parallel} = \frac{[D_H(\bar{z})/r_s]}{[D_H(\bar{z})/r_s]_{\rm fid}} \ , \qquad \alpha_{\perp} = \frac{[D_A(\bar{z})/r_s]}{[D_A(\bar{z})/r_s]_{\rm fid}} \ , \tag{4.3}$$

where r_s is the sound horizon, $D_H(z) = c/H(z)$ is the Hubble distance, and $D_A(z)$ the comoving angular diameter distance. The mean redshift of our measurement is $\bar{z} = 2.36$.

The scale factors ($\alpha_{\parallel}$,$\alpha_{\perp}$) only appear in the *peak* part of the correlation, to ensure that no information comes from the broadband shape. A detailed description of the decomposition of the cosmological signal into a *peak* and a *smooth* component can be found in [19].

4.1.1 Theoretical model for the cross-correlation

We model the *cosmological* correlation $\xi_{\rm cosmo}(\mathbf{r})$ as the 3D Fourier transform of the cross-power spectrum $P_{qF}(\mathbf{k})$:

$$P_{qF}(\mathbf{k}) = b_q \left[1 + \beta_q \mu_k^2\right] b_F \left[1 + \beta_F \mu_k^2\right] \ P(k) \ , \tag{4.4}$$

where b_q is the linear bias of quasars, b_F the linear bias of Lyα forest, and β_q and β_F the redshift space distortion parameters for quasars and Lyα forest. The matter power spectrum is $P(k)$, which includes the non-linear broadening of the peak [19] and μ_k is the cosine of the angle between the Fourier mode vector $\mathbf{k}$ and the line of sight.

Following [20] we leave two of the four bias parameters free (b_q and β_F) and derive the other two from them, using the well-constrained combination $b_F(1 + \beta_F) = -0.336 \pm 0.03$ [15] and the Kaiser relation $b_q\beta_q = f(\Omega_m)$ [42], where $f(\Omega_m)$ is the logarithmic growth rate of structure. Note that the same relation does not apply to the Lyα forest (e.g., [15]). These values of the bias parameters are defined at $z = 2.25$, and we translate them to our mean redshift $\bar{z} = 2.36$ assuming that only b_F evolves with redshift, following $(b_F(z)g(z))^2 \propto (1 + z)^{3.8}$, where $g(z)$ is the linear growth factor (as discussed in [15]).

4.1.2 Quasar redshift errors

Determining precise quasar redshifts is a difficult task. As noted in [20], quasar redshift errors have two main effects on the cross-correlation: a) the r.m.s. in the quasar redshift estimates ($\sigma_z \sim 500\,{\rm km\,s^{-1}}$) smooths the cross-correlation along the line of sight (with an equivalent effect on the quasar auto-correlation, [21]); b) a systematic offset in the BOSS redshift estimates shifts the cross-correlation along the line of sight by a non-negligible amount $\Delta_z \sim -180\,{\rm km\,s^{-1}}$ (see [20]).

Since we restrict our analysis to large separations ($r > 40\,h^{-1}\,{\rm Mpc}$), we do not expect quasar redshift errors to have a significant impact on our fits. We leave Δ_z as a free parameter in all our fits, presenting our results after marginalizing over it. We do not include an explicit σ_z parameter since it would be highly degenerate with the non-linear broadening model.

	β_F	b_q	$a_{\rm peak}$	α	$\alpha_\parallel$	$\alpha_\perp$	χ^2 (d.o.f)
FID	1.09 ± 0.29	3.02 ± 0.22	-	-	1.042 ± 0.034	0.930 ± 0.036	426.4 (420)
ISO	1.09 ± 0.30	3.00 ± 0.22	-	0.988 ± 0.022	-	-	429.5 (421)
NW	1.13 ± 0.34	2.71 ± 0.21	-	-	-	-	448.5 (422)
AMP	1.14 ± 0.32	3.02 ± 0.22	1.15 ± 0.24	-	1.041 ± 0.033	0.933 ± 0.035	426.0 (419)
PCA	1.54 ± 0.42	3.14 ± 0.22	-	-	1.052 ± 0.035	0.922 ± 0.044	474.7 (420)

Table 1: Best fit parameters for different analyses : fiducial BAO fit (FID), istropic BAO fit (ISO), non-BAO fit (NW), fit with free amplitude (AMP) and using a continuum fitting method based on a Principal Component Analysis (PCA, [40]).

4.1.3 Broadband distortion

All BAO analyses to date have used a broadband model that parameterizes each multipole as a function of r, or a parameterization as a function of (r,μ) as in [18]. However, the shape of the distortion discussed in section 3.4 that is introduced into the cross-correlation by the continuum fitting operation is better separated in terms of the $(r_\parallel, r_\perp)$ coordinates, as inferred from the analysis that was presented in [39] (see their figure 17). In this figure, one can see that the distortion decreases rapidly with $r_\perp$, and it has a non-trivial $r_\parallel$ dependence. Therefore, we use the following parameterization for the broadband distortion model:

$$\xi_{bb}(r_\parallel, r_\perp) = \sum_{i=i_{min}}^{i_{max}} \sum_{j=j_{min}}^{j_{max}} b_{ij}\ r_\parallel^i\ r_\perp^j\ , \tag{4.5}$$

where the sums are understood to be over consecutive integers, and they go from $i_{\rm min} = 0$ to $i_{\rm max} = 2$, and from $j_{\rm min} = -3$ to $j_{\rm max} = 1$ in our fiducial analysis. The dependence of our results on the broadband distortion model is discussed in section 4.3.

4.2 BAO fits

Our fiducial BAO fit is performed over the separation range $40\,h^{-1}\,{\rm Mpc} < r < 180\,h^{-1}\,{\rm Mpc}$ using a broadband model with ($i_{min} = 0$, $i_{max} = 2$, $j_{min} = -3$, $j_{max} = 1$). The total number of bins included is 440, and the number of free parameters is 20: $\alpha_\parallel$, $\alpha_\perp$, β_F, b_q, Δ_z and the 15 parameters b_{ij} in our broadband distortion model. In table 1 we present the best fit values for our fiducial analysis, and for a series of illustrative alternative analyses: an isotropic BAO analysis (ISO) imposing $\alpha \equiv \alpha_\parallel = \alpha_\perp$; a no-wiggles fit (NW) with $a_{\rm peak} = 0$; a fit allowing the amplitude of the peak $a_{\rm peak}$ to vary (AMP); and a fit using a different method to fit the continua based on a Principal Component Analysis (PCA, [40]).

The BAO peak position is significantly measured to an accuracy better than $\sim 4\%$ both along and across the line of sight directions. The measured amplitude of the BAO peak is consistent with the expected in our fiducial model.

In figure 3 we present the main result of this paper: the value of $\Delta\chi^2$ as a function of $(\alpha_\parallel,\alpha_\perp)$ for our fiducial BAO analysis, fully marginalized over the other 18 free parameters. The solid contours correspond to $\Delta\chi^2 = 2.27$, 5.99 and 11.62, equivalent to likelihood contours of 68%, 95% and 99.7% for a Gaussian likelihood. The fiducial model is consistent at the $\sim 1.5\sigma$ level.

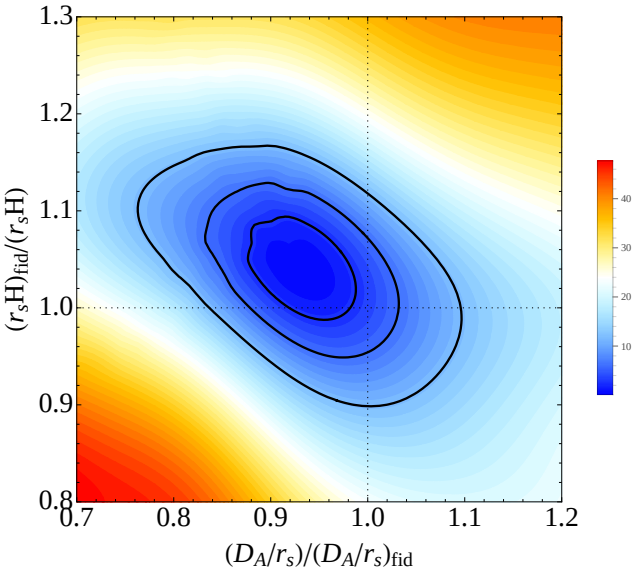

Figure 3: $\Delta\chi^2$ as a function of $\alpha_{\parallel}$,$\alpha_{\perp}$ (defined in equation 4.3) in our fiducial analysis, after marginalizing over the remaining 18 parameters. The solid contours correspond to $\Delta\chi^2 = 2.27$, 5.99 and 11.62, equivalent to Gaussian probabilities of 68%, 95% and 99.7%. The fiducial model is consistent at the $\sim 1.5\sigma$ level.

We can translate our measurement of ($\alpha_{\parallel}$,$\alpha_{\perp}$) to a measurement of the Hubble parameter and the angular diameter distance at our mean redshift $z = 2.36$, up to a factor r_s:

$$c/(H(z = 2.36)\ r_s) = 9.0 \pm 0.3\ , \qquad D_A(z = 2.36)\ /\ r_s = 10.8 \pm 0.4\ . \tag{4.6}$$

Using the best fit value of the sound horizon from the Planck collaboration ($r_s = 147.49\,\mathrm{Mpc}$) [3] [3], we can present the results as:

$$H(z = 2.36) = 226 \pm 8\,\mathrm{km\,s^{-1}\,Mpc^{-1}} \qquad D_A(z = 2.36) = 1590 \pm 60\,\mathrm{Mpc}\ . \tag{4.7}$$

4.3 Systematic tests

Table 2 presents the dependence of our results on the broadband model for our fiducial analysis. We start by presenting the results in the absence of any broadband distortion term (NO BB row), and we increasingly add more free parameters to our model in an attempt to remove the distortion caused by the continuum fitting method (see Figure 17 of [39]). Adding a single constant (BB_0) does not improve the fit, but adding a $r_{\perp}^{-1}$ term reduces the best fit χ^2 by 30. The goodness of fit keeps improving while adding new free parameters, until it saturates close to our fiducial model (BB_7), after which adding new parameters does not improve the fit much. The BAO results are very insensitive to the chosen broadband function form for all models with more than 6 free parameters (BB_4 - BB_14), and even the model with only 2 free parameters gives very similar results.

[3]Table 2, column with 68% limits for Planck+WP.

Model	N_{bb}	β_F	b_q	$\alpha_\parallel$	$\alpha_\perp$	χ^2 Prob
NO BB (-)	0	2.85 ± 0.62	2.75 ± 0.16	1.049 ± 0.039	0.902 ± 0.048	0.056
BB_0 (0, 0, 0, 0)	1	2.87 ± 0.62	2.75 ± 0.16	1.050 ± 0.039	0.902 ± 0.048	0.054
BB_1 (0, 0, -1, 0)	2	1.55 ± 0.30	2.73 ± 0.16	1.038 ± 0.039	0.921 ± 0.041	0.255
BB_2 (0, 1, -1, 0)	4	1.51 ± 0.29	2.75 ± 0.16	1.039 ± 0.038	0.921 ± 0.040	0.254
BB_3 (0, 2, -1, 0)	6	1.22 ± 0.25	2.94 ± 0.18	1.047 ± 0.036	0.916 ± 0.040	0.318
BB_4 (0, 2, -2, 0)	9	0.91 ± 0.22	3.11 ± 0.20	1.044 ± 0.035	0.927 ± 0.037	0.350
BB_5 (0, 2, -2, 1)	12	0.95 ± 0.23	3.14 ± 0.21	1.043 ± 0.034	0.933 ± 0.036	0.397
BB_6 (0, 2, -3, 0)	12	0.94 ± 0.24	3.05 ± 0.22	1.047 ± 0.035	0.924 ± 0.037	0.381
BB_7 (0, 2, -3, 1)	15	1.09 ± 0.29	3.02 ± 0.22	1.042 ± 0.034	0.930 ± 0.036	0.404
BB_8 (0, 3, -2, 1)	16	0.88 ± 0.22	3.14 ± 0.21	1.043 ± 0.033	0.932 ± 0.036	0.467
BB_9 (0, 3, -3, 1)	20	1.01 ± 0.27	3.01 ± 0.22	1.042 ± 0.034	0.929 ± 0.036	0.463
BB_10 (-1, 3, -2, 1)	20	0.89 ± 0.22	3.14 ± 0.21	1.045 ± 0.033	0.931 ± 0.036	0.443
BB_11 (0, 4, -2, 1)	20	0.74 ± 0.18	3.23 ± 0.26	1.052 ± 0.034	0.930 ± 0.035	0.525
BB_12 (0, 5, -2, 1)	24	0.80 ± 0.23	3.17 ± 0.27	1.051 ± 0.034	0.932 ± 0.035	0.517
BB_13 (0, 4, -2, 2)	25	0.75 ± 0.21	3.15 ± 0.28	1.052 ± 0.034	0.923 ± 0.035	0.514
BB_14 (0, 4, -3, 1)	25	0.90 ± 0.27	3.03 ± 0.28	1.047 ± 0.035	0.929 ± 0.036	0.513

Table 2: Best fit parameters for different broadband distortion models, defined by their values of (i_{min},i_{max},j_{min},j_{max}) in equation 4.5. N_{bb} is the total of free parameters of the broadband distortion model. The last column shows the probability inferred from the χ^2 value in the fit and the number of degrees of freedom (different in each row). The first row (NO BB) shows the results for a fit without distortion, and row BB_7 corresponds to our fiducial model.

Table 3 presents the dependence on the separation range over which the cross-correlation is fitted, when the maximum separation is modified from the fiducial value of $180\,h^{-1}$ Mpc to $170\,h^{-1}$ Mpc (RMAX_170) or to $190\,h^{-1}$ Mpc (RMAX_190), and the minimum separation from $40\,h^{-1}$ Mpc to $30\,h^{-1}$ Mpc (RMIN_30) or to $50\,h^{-1}$ Mpc (RMIN_50). The last three rows show the results of restricting the range of the angle cosine $\mu = r_\parallel/r$ to $\|\mu\| < 0.8$ (MU_08), $\|\mu\| < 0.9$ (MU_09), or $\|\mu\| < 0.95$ (MU_095). The results in this table show that the BAO measurement in general has little dependence on the fitting range. The broadband distortion is most important for separations near the line of sight (i.e., $\|\mu\|$ near one), but the removal of this most contaminated part does not significantly alter the BAO peak position that is obtained, except in the MU_095 case where the position that is obtained shifts to a value closer to the expected one in our fiducial model by nearly 1σ.

4.4 Test of the covariance matrix

In table 1 we can see that the χ^2 value in our fiducial fit is good, in the sense that it is compatible with being drawn from a χ^2 distribution with mean equal to the degrees of freedom in the problem, i.e., the number of bins used in the fit (440) minus the number of free parameters (20).

In order to test our estimate of the covariance matrix, we examine the distribution of χ^2 for its different eigenmodes. The results of this test are compared to a zero-mean Gaussian with variance $(440 - 20)/440$ in figure 4. The agreement supports the validity of our covariance matrix.

	β_F	b_q	$\alpha_\parallel$	$\alpha_\perp$	χ^2 (d.o.f)
FID	1.09 ± 0.29	3.02 ± 0.22	1.042 ± 0.034	0.930 ± 0.036	426.4 (420)
RMAX_170	1.07 ± 0.28	3.07 ± 0.22	1.046 ± 0.034	0.926 ± 0.036	397.4 (394)
RMAX_190	1.05 ± 0.27	3.04 ± 0.22	1.042 ± 0.034	0.929 ± 0.036	438.3 (436)
RMIN_30	1.03 ± 0.21	2.85 ± 0.14	1.043 ± 0.035	0.930 ± 0.038	443.5 (430)
RMIN_50	1.65 ± 0.71	3.01 ± 0.34	1.044 ± 0.034	0.923 ± 0.038	407 (406)
MU_08	2.26 ± 2.0	2.61 ± 0.38	1.025 ± 0.088	0.937 ± 0.055	257.1 (244)
MU_09	1.39 ± 0.89	2.73 ± 0.41	1.023 ± 0.054	0.938 ± 0.041	306.7 (302)
MU_095	0.88 ± 0.32	3.13 ± 0.27	1.009 ± 0.041	0.949 ± 0.037	353.6 (344)

Table 3: Best fit parameters for the fiducial analysis (FID), and different fitting ranges (in h^{-1} Mpc). The last rows show the results when using only bins that are far from the line of sight, with $|\mu| < 0.8$ (MU_08), $|\mu| < 0.9$ (MU_09) and $|\mu| < 0.95$ (MU_095).

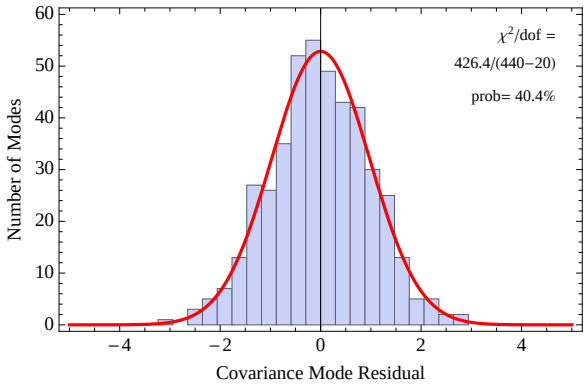

Figure 4: Histogram of χ^2 values for the different eigenmodes of the covariance matrix, compared to a zero-mean Gaussian with variance $(440 - 20)/440$, where 440 is the number of bins in the fit, and 20 is the number of free parameters. The agreement between the distributions supports the validity of our covariance matrix.

4.5 Alternative uncertainty estimates of the BAO scales

The error on the fitted parameters reported so far have been computed from the second derivatives of the log-likelihood function at its maximum, assuming this likelihood function to be Gaussian at 1σ. The BAO scale uncertainties in the fiducial analysis obtained in this way are 0.034 for $\alpha_\parallel$ and 0.036 for $\alpha_\perp$. An alternative error estimate can be computed from the full likelihood surface in figure 3, without assuming a Gaussian likelihood. The uncertainties obtained in the fiducial analysis are then 0.032 for $\alpha_\parallel$ and 0.036 for $\alpha_\perp$, in good agreement with the previous ones.

Both these estimates rely on the accuracy of the covariance matrix that we have computed as described in section 3. We test this by computing an alternative bootstrap error on the BAO scale parameters, that does not rely on our covariance matrix. We generate 1,000 bootstrap realizations of the survey [43], combining the measurements from the 66 different sub-samples. The fitting analysis is done for each realization, and the uncertainties on $\alpha_\parallel$ and $\alpha_\perp$ are computed from their distribution of best fit values. The resulting uncertainties

on the BAO scales are 0.031 on $\alpha_\parallel$ and 0.036 on $\alpha_\perp$, in excellent agreement with the previous estimates.

4.6 Visualizing the BAO Peak

Even though we do not use multipoles anywhere in our analysis, we present here a fit of the multipoles from the measured cross-correlation in order to better *see* the BAO peak in the data. We start by constructing a multipole expansion of our measured cross-correlation, $\xi(r_\parallel, r_\perp)$, using a linear least-squares fit to:

$$\xi(r,\mu) = \sum_l L_l(\mu)\xi_l(r) \ , \tag{4.8}$$

where $r = \sqrt{r_\parallel^2 + r_\perp^2}$ and $\mu = r_\parallel/r$, $L_l(x)$ is the Legendre polynomial of order l and $\xi_l(r)$ are the multipoles we wish to measure.

In figure 2 we show the measured cross-correlation, as a function of line of sight ($r_\parallel$) and transverse ($r_\perp$) separation, together with our best fit model. From the right panel of the figure, one can see that the best fit model of the broadband distortion is asymmetric with respect to $r_\parallel = 0$. Therefore we expect a net non-zero contribution from odd multipoles. For the purpose of visualization, however, we only fit the monopole ($l = 0$) and the quadrupole ($l = 2$), since these two multipoles contain most of the cosmological infomation. We use 36 equidistant interpolation points separated by $4\,h^{-1}$ Mpc and ranging from $40\,h^{-1}$ Mpc to $180\,h^{-1}$ Mpc.

Our estimates of the multipoles at different separations are highly correlated. In order to improve the visualization of the BAO peak, we apply a correction to the multipoles based on the analysis presented in [19]. We start by examining the eigenmodes of the covariance matrix and identify a particular mode being essentially a DC offset of the monopole, and therefore responsible for much of the correlations between separations. We then project out the mode from the data and its covariance matrix, and refit for the distortion while keeping all other parameters fixed from the baseline best fit.

Figure 5 shows the resulting monopole and quadrupole of the quasar-Lyα cross-correlation, expressed as the transverse correlation, $\xi(r, \mu = 0) = \xi_0(r) - \xi_2(r)/2$ (left panel), and the parallel correlation $\xi(r, \mu = 1) = \xi_0(r) + \xi_2(r)$. We superimpose a fit with all parameters fixed from the 2D BAO fit except for the distortion. The solid black curve shows the best fit, the red dashed curve is the BAO-only part (with parameters fixed from the 2D fit), and the green dotted curve shows the distortion, which is parabolic after r^2 weighting. Since the Lyα fluctuation is defined in equation 3.4 as a transmission fluctuation, positive values of δ_F reflect negative density fluctuations, implying a negative value for the bias factor b_F. This explains why the BAO feature in the quasar-Lyα cross-correlation appears as a dip instead of a peak, as seen in figure 5.

The orange curve in figure 5 shows the predicted cross-correlation for our fiducial cosmological model with $\alpha_\parallel = \alpha_\perp = 1$, and an amplitude determined by a quasar bias factor $b_q = 3.64$ and a Lyα redshift distortion parameter $\beta_F = 1.1$, as measured in [20]. The fact that this model is consistent with the best fit that is obtained here to the DR11 data proves that our result is consistent with that obtained in [20] using the DR9 data, and that the

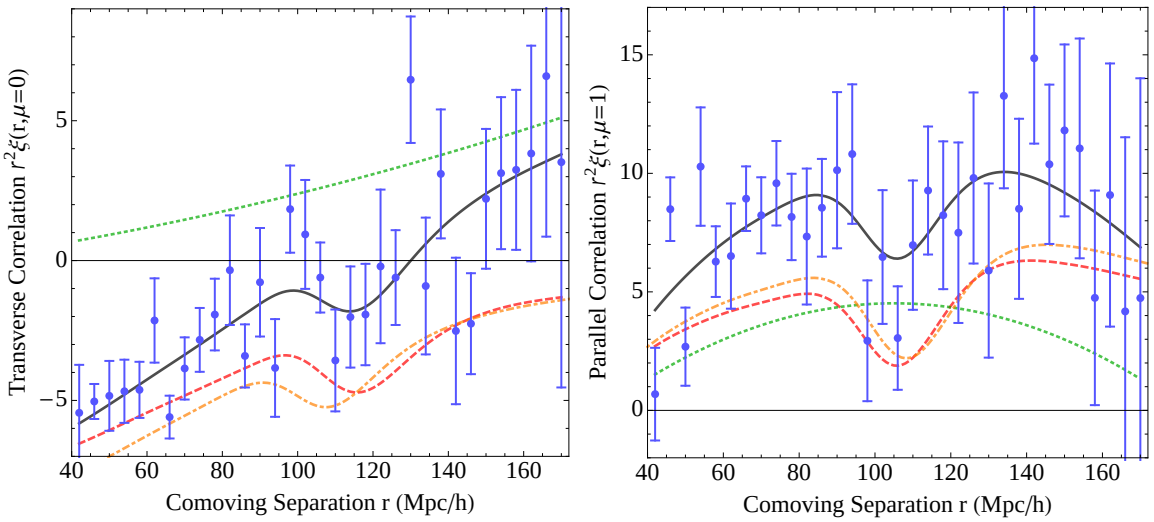

Figure 5: Transverse (left) and parallel (right) correlations, defined as $\xi(r,\mu=0)=\xi_0(r)-\xi_2(r)/2$ and $\xi(r,\mu=1)=\xi_0(r)+\xi_2(r)$, after projecting out the mode responsible for most of the correlation between separations. The best fit theory is shown in a solid black curve, its BAO-only part in a red dashed curve and the distortion in a dotted green curve. The orange dot-dashed curve shows the cosmological signal for our fiducial cosmology ($\alpha=1$), using a quasar bias of $b_q=3.64$ and a Lyα redshift-space distortion parameter $\beta_F=1.1$, as measured in [20]. All datapoints and lines are weighted by r^2 and are plotted after the projection (see text for details).

different values that are obtained in our fit for b_q and β_F are caused by our addition of an arbitrary broadband function, with parameters that are degenerate with b_q and β_F. The amplitude of the BAO dip, as visualized in figure 5, is consistent with our expectation. This is seen also in the model AMP in table 1, where the parameter $a_{\rm peak}$ has a best fit value that is consistent with unity. A model with a suppressed BAO peak (model NW in table 1) has a χ^2 that is worse than our fiducial model by 20, although we warn that this is not to be directly interpreted as a statistical significance of a BAO detection because our likelihood function is not necessarily Gaussian. In any case, our interest here lies in the statistical constraint obtained on the BAO scale, rather than the significance of the BAO detection in the quasar-Lyα cross-correlation only.

5 Discussion & Conclusions

We have presented a measurement of the quasar - Lyα cross-correlation using approximately 164,000 quasars from the eleventh Data Release (DR11) of SDSS. We are able to measure the BAO scale along and across the line of sight ($\alpha_\parallel$, $\alpha_\perp$) with an uncertainty of 3.4% and 3.6% respectively. The measurement is in agreement with our fiducial cosmology well within the 95% confidence level.

We have checked the robustness of our measurement under changes of broadband mod-

els, separation range used, and different error estimates. As discussed in section 3.4, we are not particularly careful in our treatment of the non-BAO part of the cross-correlation. However, the best fit values for the bias parameters of both quasars and Lyα forest are roughly consistent with previous analyses, with rather large uncertainties since we only use large separations to measure the BAO scale.

In table 4 we compare the results with other BAO measurements at the same redshift from the Lyα auto-correlation measured with DR9 ([17], [18]). We also present our results when using only data from DR10. Assuming that the uncertainties in these BAO measurements scale with the inverse of the square root of the survey area, we can extrapolate them from DR9 to DR11, using $\sqrt{A_{DR11}/A_{DR9}} = 1.60$. We show these extrapolations in the last two rows of table 4.

Analysis	Probe	Data Release	α	$\alpha_{\parallel}$	$\alpha_{\perp}$
Busca_2013	Auto	DR9	1.01 ± 0.03	-	-
Slosar_2013	Auto	DR9	0.98 ± 0.020	0.99 ± 0.035	0.98 ± 0.070
This work	Cross	DR10	1.00 ± 0.027	1.06 ± 0.038	0.91 ± 0.041
This work	Cross	DR11	0.99 ± 0.022	1.04 ± 0.034	0.93 ± 0.036
Busca_2013	Auto	to DR11	± 0.019	-	-
Slosar_2013	Auto	to DR11	± 0.013	± 0.022	± 0.046

Table 4: Comparison of different BAO analysis at $z \sim 2.4$ from BOSS, from the auto-correlation in DR9 (Busca_2013 [17], Slosar_2013 [18]), and from this work. We show our results when using only DR10 data and when including DR11 data. In the last two rows we extrapolate the uncertainties of previous work to DR11, assuming that these scale with the inverse of the square root of the survey area.

The errors on the BAO scale ($\alpha_{\parallel}$,$\alpha_{\perp}$) from our DR10 analysis are considerably smaller than those reported in [44]. An extensive comparison of the two analyses within the BOSS Lyα working group concluded that the discrepancy can be explained by the differences in the analysis. While [44] uses only the monopole and the quadrupole to fit the BAO scale, in this analysis we use the full 2D contours of the cross-correlation function.

In the absence of any broadband distortion of $\xi(r_{\parallel}, r_{\perp})$ (or with a distortion that is a-priori known), we find that essentially all of the BAO signal is contained within the monopole $\xi_0(r)$ and quadrupole $\xi_2(r)$. However, when broadband distortion is present, as in our analysis, it contributes significantly to multipoles other than the monopole and quadrupole, and leads to correlated uncertainties between distortion and BAO parameters and corresponding parameter degeneracies. As a result, we find that the unknown broadband distortion parameters can be determined more precisely with a fit to the full $\xi(r_{\parallel}, r_{\perp})$ (or, equivalently, a larger set of multipoles) instead of a fit to only the monopole and quadrupole. Similarly, we find that a fit to $\xi(r_{\parallel}, r_{\perp})$ yields a more precise determination of the BAO parameters by helping to break the degeneracy between distortion and BAO parameters. The actual improvement we find is a factor of 1.2 in $\alpha_{\parallel}$ and a factor of 1.3 in $\alpha_{\perp}$. [36] found that a similar improvement is also seen when measuring BAO from the Lyα auto-correlation function, although a detailed study on mock data sets revealed a large scatter in the gain from realization to realization.

5.1 Lyα auto-correlation vs. quasar-Lyα cross-correlation

In appendix B we present a Fisher matrix projection comparing the relative strength of measuring BAO with the Lyα auto-correlation and with the quasar-Lyα cross-correlation. In a BOSS-like survey, both probes should measure the transverse BAO scale with similar uncertainties, while the Lyα auto-correlation should be able to measure the line of sight scale $\sim 40\%$ better than the cross-correlation with quasars.

The measurement of BAO from the Lyα auto-correlation in DR9 was presented in [17] and [18]. Most of the difference between the uncertainties in these results can be explained by the looser data cuts used in [18], that included lines with DLAs and that defined their Lyα forest with a wider wavelength range. In this analysis we used data cuts similar to those in [18], and therefore we compare here our uncertainties with those from [18] extrapolated to DR11 (see table 4).

Our measurement of $\alpha_{\parallel}$ is $\sim 55\%$ worse than the results from the Lyα auto-correlation of [18] extrapolated to DR11, in good agreement with the prediction of $\sim 40\%$ computed in the appendix. The Fisher forecast formalism predicted similar uncertainties in $\alpha_{\perp}$, and we find that our measurement is $\sim 20\%$ better than the extrapolated results from the auto-correlation.

In the same appendix we also show that on the scales of interest for BAO measurements ($k > 0.05\,h\,\mathrm{Mpc}^{-1}$) cosmic variance is not the dominant contribution to our error budget. Assuming that the shot noise in the quasar density field is uncorrelated with the small scale fluctuations in the Lyα absorption and with the instrumental noise, we can then combine both BAO measurements as if they were independent.

In figure 6 we compare the contours on ($\alpha_{\parallel}$,$\alpha_{\perp}$) from the Lyα auto-correlation function from DR9 ([18] in blue, generated from the files in `http://darkmatter.ps.uci.edu/baofit/`), and compare it to our measurement from the cross-correlation function from DR11 (red) and the sum of their χ^2 surfaces (in black), assuming they are independent. We compare these constraints with the 68% and 95% confidence limits obtained from the Planck results [3] in an open ΛCDM cosmology, shown in green. [4] Note that by allowing for space curvature, the Planck constraints on the distance and expansion rate at our mean redshift $z = 2.36$ are much less restrictive compared to a flat model.

We have shown that adding the cross-correlation of Lyα and quasars to the auto-correlation of Lyα can certainly improve the constraints on BAO scales at high redshfit. A detailed analysis of the cosmological implications of the measurements of the Lyα auto-correlation and the quasar-Lyα cross-correlation will be presented in a future publication, which will include the DR11 results from the Lyα auto-correlation, together with a more complete examination of potential correlations between the two measurements.

Acknowledgments

We would like to thank Ross O'Connell for detailed comparisons with his analysis, and Shirley Ho for very useful comments.

[4] We use the Planck + ACT/SPT + WP public chains available under the name base_omegak_planck_lowl_lowLike_highL.

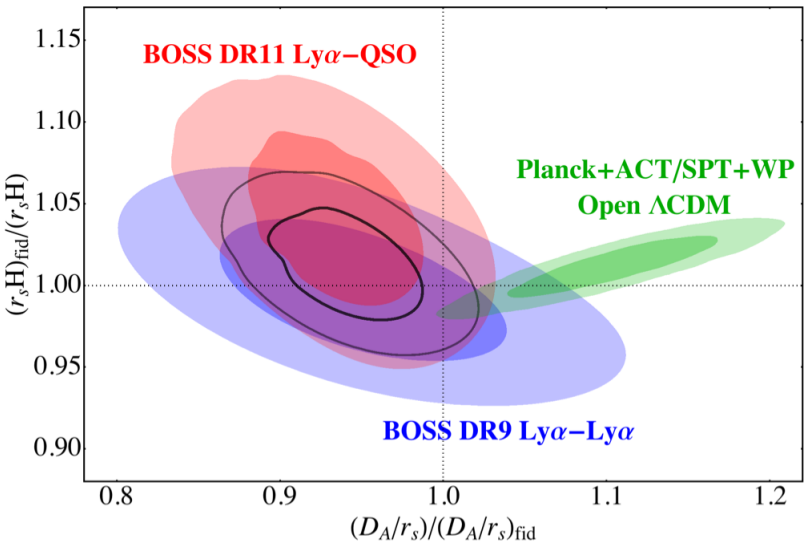

Figure 6: Contours of $\Delta\chi^2 = 2.27$ and 5.99, corresponding to Gaussian confidence levels of 68% and 95%, from the Lyα auto-correlation analysis from DR9 ([18], in blue), from the cross-correlation from DR11 (this work, in red) and from the joint analysis (in black). The green contours show the 68% and 95% contours for the regions of this parameter space allowed by the Planck results [3] in an open ΛCDM cosmology.

This research used resources of the National Energy Research Scientific Computing Center (NERSC), which is supported by the Office of Science of the U.S. Department of Energy under Contract No. DE-AC02-05CH11231. DK would like to thank CEA Saclay for their hospitality and productive environment during his sabbatical. JM is supported in part by Spanish grant AYA2012-33938.

Funding for SDSS-III has been provided by the Alfred P. Sloan Foundation, the Participating Institutions, the National Science Foundation, and the U.S. Department of Energy Office of Science. The SDSS-III web site is http://www.sdss3.org/.

SDSS-III is managed by the Astrophysical Research Consortium for the Participating Institutions of the SDSS-III Collaboration including the University of Arizona, the Brazilian Participation Group, Brookhaven National Laboratory, University of Cambridge, Carnegie Mellon University, University of Florida, the French Participation Group, the German Participation Group, Harvard University, the Instituto de Astrofisica de Canarias, the Michigan State/Notre Dame/JINA Participation Group, Johns Hopkins University, Lawrence Berkeley National Laboratory, Max Planck Institute for Astrophysics, Max Planck Institute for Extraterrestrial Physics, New Mexico State University, New York University, Ohio State University, Pennsylvania State University, University of Portsmouth, Princeton University, the Spanish Participation Group, University of Tokyo, University of Utah, Vanderbilt University, University of Virginia, University of Washington, and Yale University.

References

[1] A. G. Riess, A. V. Filippenko, P. Challis, A. Clocchiatti, A. Diercks, P. M. Garnavich, R. L. Gilliland, C. J. Hogan, S. Jha, R. P. Kirshner, *et al.*, AJ **116**, 1009 (Sep. 1998), arXiv:astro-ph/9805201.

[2] S. Perlmutter, G. Aldering, G. Goldhaber, R. A. Knop, P. Nugent, P. G. Castro, S. Deustua, S. Fabbro, A. Goobar, D. E. Groom, *et al.*, *Astrophys. J.* **517**, 565 (Jun. 1999), arXiv:astro-ph/9812133.

[3] Planck Collaboration, P. A. R. Ade, N. Aghanim, C. Armitage-Caplan, M. Arnaud, M. Ashdown, F. Atrio-Barandela, J. Aumont, C. Baccigalupi, A. J. Banday, *et al.*, ArXiv e-prints (Mar. 2013), 1303.5076.

[4] D. H. Weinberg, M. J. Mortonson, D. J. Eisenstein, C. Hirata, A. G. Riess, and E. Rozo, ArXiv e-prints (Jan. 2012), 1201.2434.

[5] H.-J. Seo and D. J. Eisenstein, *Astrophys. J.* **598**, 720 (Dec. 2003).

[6] D. J. Eisenstein, I. Zehavi, D. W. Hogg, R. Scoccimarro, M. R. Blanton, R. C. Nichol, R. Scranton, H.-J. Seo, M. Tegmark, Z. Zheng, *et al.*, *Astrophys. J.* **633**, 560 (Nov. 2005).

[7] S. Cole, W. J. Percival, J. A. Peacock, P. Norberg, C. M. Baugh, C. S. Frenk, I. Baldry, J. Bland-Hawthorn, T. Bridges, R. Cannon, *et al.*, *Mon. Not. Roy. Astron. Soc.* **362**, 505 (Sep. 2005), arXiv:astro-ph/0501174.

[8] C. Blake, E. A. Kazin, F. Beutler, T. M. Davis, D. Parkinson, S. Brough, M. Colless, C. Contreras, W. Couch, S. Croom, *et al.*, *Mon. Not. Roy. Astron. Soc.* **418**, 1707 (Dec. 2011), 1108.2635.

[9] L. Anderson, E. Aubourg, S. Bailey, D. Bizyaev, M. Blanton, A. S. Bolton, J. Brinkmann, J. R. Brownstein, A. Burden, A. J. Cuesta, *et al.*, *Mon. Not. Roy. Astron. Soc.* **427**, 3435 (Dec. 2012), 1203.6594.

[10] A. Merloni, P. Predehl, W. Becker, H. Böhringer, T. Boller, H. Brunner, M. Brusa, K. Dennerl, M. Freyberg, P. Friedrich, *et al.*, ArXiv e-prints (Sep. 2012), 1209.3114.

[11] J. C. Pober, A. R. Parsons, D. R. DeBoer, P. McDonald, M. McQuinn, J. E. Aguirre, Z. Ali, R. F. Bradley, T.-C. Chang, and M. F. Morales, AJ **145**, 65, 65 (Mar. 2013), 1210.2413.

[12] G. J. Hill, K. Gebhardt, E. Komatsu, N. Drory, P. J. MacQueen, J. Adams, G. A. Blanc, R. Koehler, M. Rafal, M. M. Roth, *et al.*, in T. Kodama, T. Yamada, and K. Aoki, eds., *Astronomical Society of the Pacific Conference Series* (Oct. 2008), vol. 399 of *Astronomical Society of the Pacific Conference Series*, pp. 115–+.

[13] D. J. Schlegel, C. Bebek, H. Heetderks, S. Ho, M. Lampton, M. Levi, N. Mostek, N. Padmanabhan, S. Perlmutter, N. Roe, *et al.*, ArXiv e-prints (Apr. 2009), 0904.0468.

[14] G. Zhao and collaborators, *The Extended BOSS Survey (eBOSS)*, in preparation (2013).

[15] A. Slosar, A. Font-Ribera, M. M. Pieri, J. Rich, J.-M. Le Goff, É. Aubourg, J. Brinkmann, N. Busca, B. Carithers, R. Charlassier, *et al.*, *JCAP* **9**, 1 (Sep. 2011), 1104.5244.

[16] C. P. Ahn, R. Alexandroff, C. Allende Prieto, S. F. Anderson, T. Anderton, B. H. Andrews, É. Aubourg, S. Bailey, E. Balbinot, R. Barnes, *et al.*, *Astrophys. J. Sup.* **203**, 21, 21 (Dec. 2012), 1207.7137.

[17] N. G. Busca, T. Delubac, J. Rich, S. Bailey, A. Font-Ribera, D. Kirkby, J.-M. Le Goff, M. M. Pieri, A. Slosar, É. Aubourg, *et al.*, A&A **552**, A96, A96 (Apr. 2013), 1211.2616.

[18] A. Slosar, V. Iršič, D. Kirkby, S. Bailey, N. G. Busca, T. Delubac, J. Rich, É. Aubourg, J. E. Bautista, V. Bhardwaj, *et al.*, *JCAP* **4**, 26, 026 (Apr. 2013), 1301.3459.

[19] D. Kirkby, D. Margala, A. Slosar, S. Bailey, N. G. Busca, T. Delubac, J. Rich, J. E. Bautista,

M. Blomqvist, J. R. Brownstein, *et al.*, *JCAP* **3**, 24, 024 (Mar. 2013), 1301.3456.

[20] A. Font-Ribera, E. Arnau, J. Miralda-Escudé, E. Rollinde, J. Brinkmann, J. R. Brownstein, K.-G. Lee, A. D. Myers, N. Palanque-Delabrouille, I. Pâris, *et al.*, *JCAP* **5**, 18, 018 (May 2013), 1303.1937.

[21] M. White, A. D. Myers, N. P. Ross, D. J. Schlegel, J. F. Hennawi, Y. Shen, I. McGreer, M. A. Strauss, A. S. Bolton, J. Bovy, *et al.*, *Mon. Not. Roy. Astron. Soc.* **424**, 933 (Aug. 2012), 1203.5306.

[22] A. Lewis, A. Challinor, and A. Lasenby, *Astrophys. J.* **538**, 473 (Aug. 2000).

[23] D. J. Eisenstein and W. Hu, *Astrophys. J.* **496**, 605 (Mar. 1998), arXiv:astro-ph/9709112.

[24] D. J. Eisenstein, D. H. Weinberg, E. Agol, H. Aihara, C. Allende Prieto, S. F. Anderson, J. A. Arns, É. Aubourg, S. Bailey, E. Balbinot, *et al.*, AJ **142**, 72 (Sep. 2011), 1101.1529.

[25] A. S. Bolton, D. J. Schlegel, É. Aubourg, S. Bailey, V. Bhardwaj, J. R. Brownstein, S. Burles, Y.-M. Chen, K. Dawson, D. J. Eisenstein, *et al.*, AJ **144**, 144, 144 (Nov. 2012), 1207.7326.

[26] J. E. Gunn, M. Carr, C. Rockosi, M. Sekiguchi, K. Berry, B. Elms, E. de Haas, Ž. Ivezić, G. Knapp, R. Lupton, *et al.*, AJ **116**, 3040 (Dec. 1998).

[27] J. E. Gunn, W. A. Siegmund, E. J. Mannery, R. E. Owen, C. L. Hull, R. F. Leger, L. N. Carey, G. R. Knapp, D. G. York, W. N. Boroski, *et al.*, AJ **131**, 2332 (Apr. 2006), arXiv:astro-ph/0602326.

[28] S. A. Smee, J. E. Gunn, A. Uomoto, N. Roe, D. Schlegel, C. M. Rockosi, M. A. Carr, F. Leger, K. S. Dawson, M. D. Olmstead, *et al.*, AJ **146**, 32, 32 (Aug. 2013), 1208.2233.

[29] D. G. York, J. Adelman, J. E. Anderson, S. F. Anderson, J. Annis, N. A. Bahcall, J. A. Bakken, R. Barkhouser, S. Bastian, E. Berman, *et al.*, AJ **120**, 1579 (Sep. 2000).

[30] K. S. Dawson, D. J. Schlegel, C. P. Ahn, S. F. Anderson, É. Aubourg, S. Bailey, R. H. Barkhouser, J. E. Bautista, A. Beifiori, A. A. Berlind, *et al.*, AJ **145**, 10, 10 (Jan. 2013), 1208.0022.

[31] N. P. Ross, A. D. Myers, E. S. Sheldon, C. Yèche, M. A. Strauss, J. Bovy, J. A. Kirkpatrick, G. T. Richards, É. Aubourg, M. R. Blanton, *et al.*, *Astrophys. J. Sup.* **199**, 3, 3 (Mar. 2012), 1105.0606.

[32] C. Yèche, P. Petitjean, J. Rich, E. Aubourg, N. Busca, J.-C. Hamilton, J.-M. Le Goff, I. Paris, S. Peirani, C. Pichon, *et al.*, A&A **523**, A14, A14 (Nov. 2010).

[33] J. A. Kirkpatrick, D. J. Schlegel, N. P. Ross, A. D. Myers, J. F. Hennawi, E. S. Sheldon, D. P. Schneider, and B. A. Weaver, *Astrophys. J.* **743**, 125, 125 (Dec. 2011), 1104.4995.

[34] J. Bovy, J. F. Hennawi, D. W. Hogg, A. D. Myers, J. A. Kirkpatrick, D. J. Schlegel, N. P. Ross, E. S. Sheldon, I. D. McGreer, D. P. Schneider, *et al.*, *Astrophys. J.* **729**, 141, 141 (Mar. 2011), 1011.6392.

[35] I. Pâris, P. Petitjean, É. Aubourg, S. Bailey, N. P. Ross, A. D. Myers, M. A. Strauss, S. F. Anderson, E. Arnau, J. Bautista, *et al.*, A&A **548**, A66, A66 (Dec. 2012), 1210.5166.

[36] T. Delubac and collaborators, *Lyman alpha BAO constraints from SDSS DR11*, in preparation (2013).

[37] P. Noterdaeme, P. Petitjean, W. C. Carithers, I. Pâris, A. Font-Ribera, S. Bailey, E. Aubourg, D. Bizyaev, G. Ebelke, H. Finley, *et al.*, A&A **547**, L1, L1 (Nov. 2012), 1210.1213.

[38] P. Noterdaeme, P. Petitjean, C. Ledoux, and R. Srianand, A&A **505**, 1087 (Oct. 2009), 0908.1574.

[39] A. Font-Ribera, J. Miralda-Escudé, E. Arnau, B. Carithers, K.-G. Lee, P. Noterdaeme, I. Pâris, P. Petitjean, J. Rich, E. Rollinde, *et al.*, *JCAP* **11**, 59, 059 (Nov. 2012), 1209.4596.

[40] K.-G. Lee, N. Suzuki, and D. N. Spergel, AJ **143**, 51, 51 (Feb. 2012).

[41] M. McQuinn and M. White, *Mon. Not. Roy. Astron. Soc.* **415**, 2257 (Aug. 2011), 1102.1752.

[42] N. Kaiser, *Mon. Not. Roy. Astron. Soc.* **227**, 1 (Jul. 1987).

[43] B. Efron and G. Gong, American Statistician **37**, 36 (1983).

[44] R. O'Connell and collaborators, *BAO in QSO-LyaF Cross-correlation*, in preparation (2013).

[45] F. James and M. Roos, Computer Physics Communications **10**, 343 (Dec. 1975).

[46] P. McDonald and D. J. Eisenstein, *Phys. Rev.* **D** **76**(6), 063009 (Sep. 2007), arXiv:astro-ph/0607122.

[47] P. McDonald, U. Seljak, S. Burles, D. J. Schlegel, D. H. Weinberg, R. Cen, D. Shih, J. Schaye, D. P. Schneider, N. A. Bahcall, *et al.*, *Astrophys. J. Sup.* **163**, 80 (Mar. 2006), arXiv:astro-ph/0405013.

A Public Access to Data and Code

The baofit software used in this paper is publicly available at https://github.com/deepzot/baofit/. The measured cross-correlation function and its covariance matrix, and the instructions to reproduce the BAO constraints presented in this paper, can be downloaded from http://darkmatter.ps.uci.edu/baofit/, together with the likehood surface used to generate Figure 3. The software is written in C++ and uses MINUIT [45] for likelihood minimization.

B Fisher Matrix Forecasts

The goal of this appendix is to compare the expected accuracy with which one should be able to measure the BAO scale from a BOSS-like survey using the Lyα auto-correlation function and the quasar-Lyα cross-correlation.

Instead of undertaking a full forecast of the uncertainty on the BAO scale, we will do a simpler comparison and evaluate the signal to noise ratio (S/N) that one should obtain for a certain Fourier mode $\mathbf{k}$. This is a fair comparison, since the uncertainty on the BAO scale should be proportional to the uncertainty on the power spectrum over the relevant BAO scales.

B.1 Auto-correlation

We start by computing the expected signal to noise ratio in the auto-correlation of Lyα and in the auto-correlation of quasars. On large scales, the signal in the auto-correlation can be described with a simple linear bias model with the Kaiser model to account for redshift space distortions:

$$P_A(\mathbf{k}) = b_A^2 \left(1 + \beta_A \mu^2\right)^2 \; P(k) \; , \tag{B.1}$$

where b_A and β_A are the linear bias parameter of the tracer A and its redshift space distortion parameter, $P(k)$ is the matter power spectrum, and μ is the cosine of the angle between the Fourier mode $\mathbf{k}$ and the line of sight.

The accuracy with which one can measure the quasar power spectrum $P_A(\mathbf{k})$ in a given bin centered at (k,μ) can be quantified by the signal to noise ratio (S/N),

$$\left(\frac{S}{N}\right)^2_A = N_k \, \frac{P_A^2(\mathbf{k})}{var[P_A(\mathbf{k})]} \; , \tag{B.2}$$

where N_k is the number of modes in the bin. Since we only care about relative performance in this appendix, we will drop any N_k and will plot signal to noise ratio per mode.

For a sample of point-like sources (for instance quasars), the variance of its measured power spectrum can be approximated by

$$var\left[P_A(\mathbf{k})\right] = 2\left(P_A(\mathbf{k}) + n_A^{-1}\right)^2 \; , \tag{B.3}$$

with n_A the number density of systems.

Since the Lyα forest is not a discrete point sampling of the underlying matter density field, but rather a non-linear transformation of a continuous sampling along discrete lines of sight, we need to use a slightly different approach. [46] computed the expected S/N in the measurement of $P_{FF}(\mathbf{k})$ in a spectroscopic survey, and highlighted the importance of the " aliasing term " due to the sparse sampling of the universe. Here we use the formalism from [41] that combines both the noise term and the aliasing term defining a noise-weighted density of lines of sight per unit area n_{eff},

$$var[P_{FF}(\mathbf{k})] = 2\left(P_{FF}(\mathbf{k}) + P^{1D}(k\mu)\; n_{eff}^{-1}\right)^2 \; , \tag{B.4}$$

where $P^{1D}(k\mu)$ is the one-dimensional flux power spectrum.

B.2 Cross-correlation

The cross correlation between the Lyα absorption and the quasar density field can be defined as

$$\langle \delta_F(\mathbf{k})\; \delta_q(\mathbf{k\prime})\rangle = (2\pi)^3 \delta^D(\mathbf{k}+\mathbf{k\prime})\; P_{qF}(\mathbf{k}) \; . \tag{B.5}$$

Again, in the linear regime we can relate the cross-correlation power spectrum with the linear power spectrum $P(k)$ using the linear bias parameters defined above,

$$P_{qF}(\mathbf{k}) = b_q\left(1+\beta_q\mu^2\right)\; b_F\left(1+\beta_F\mu^2\right) P(k) \; . \tag{B.6}$$

[41] showed that the variance in the measurement of the cross-correlation can be approximated by

$$var\left(P_{qF}(\mathbf{k})\right) = P_{qF}(\mathbf{k})^2 + \left(P_{qq}(\mathbf{k}) + n_q^{-1}\right)\left(P_{FF}(\mathbf{k}) + P^{1D}(k\mu)\; n_{eff}^{-1}\right) \; . \tag{B.7}$$

In this approximation, the expected S/N in a bin of (k,μ_k) can be approximated by

$$\left(\frac{S}{N}\right)^2_{Fg} = N_k \, \frac{P_{qF}^2(\mathbf{k})}{P_{qF}(\mathbf{k})^2 + \left(P_{qq}(\mathbf{k}) + n_q^{-1}\right)\left(P_{FF}(\mathbf{k}) + P^{1D}(k\mu)\; n_{eff}^{-1}\right)} \; . \tag{B.8}$$

B.3 Forecast for a BOSS-like survey

Here we quantify the previous results for the case of a spectroscopic survey with properties similar to the BOSS survey. The BOSS survey has an area of $A = 10^4\,\mathrm{deg}^2$, and if we restrict the analysis to the redshift range $2 < z < 3$, the total volume of the survey is roughly $V = 40(\,h^{-1}\,\mathrm{Gpc})^3$. The quasar density in the BOSS survey is roughly $n_q = 160000/V \sim 4 \times 10^{-6}(\,h^{-1}\,\mathrm{Mpc})^{-3}$, and we assume a quasar bias of $b_q = 3.6$ ([20],[21]). The effective density of lines of sight for BOSS is estimated in [41] to be $n_{eff} \approx 10^{-3}(\,h^{-1}\,\mathrm{Mpc})^{-2}$, and we assume the values for the Lyα biases of $b_F = -0.15$ and $\beta_F = 1.2$, both compatible with the 1D measurement of [47] and the 3D clustering from [15]. We compute the power spectra at our fiducial redshfit of $z_c = 2.36$.

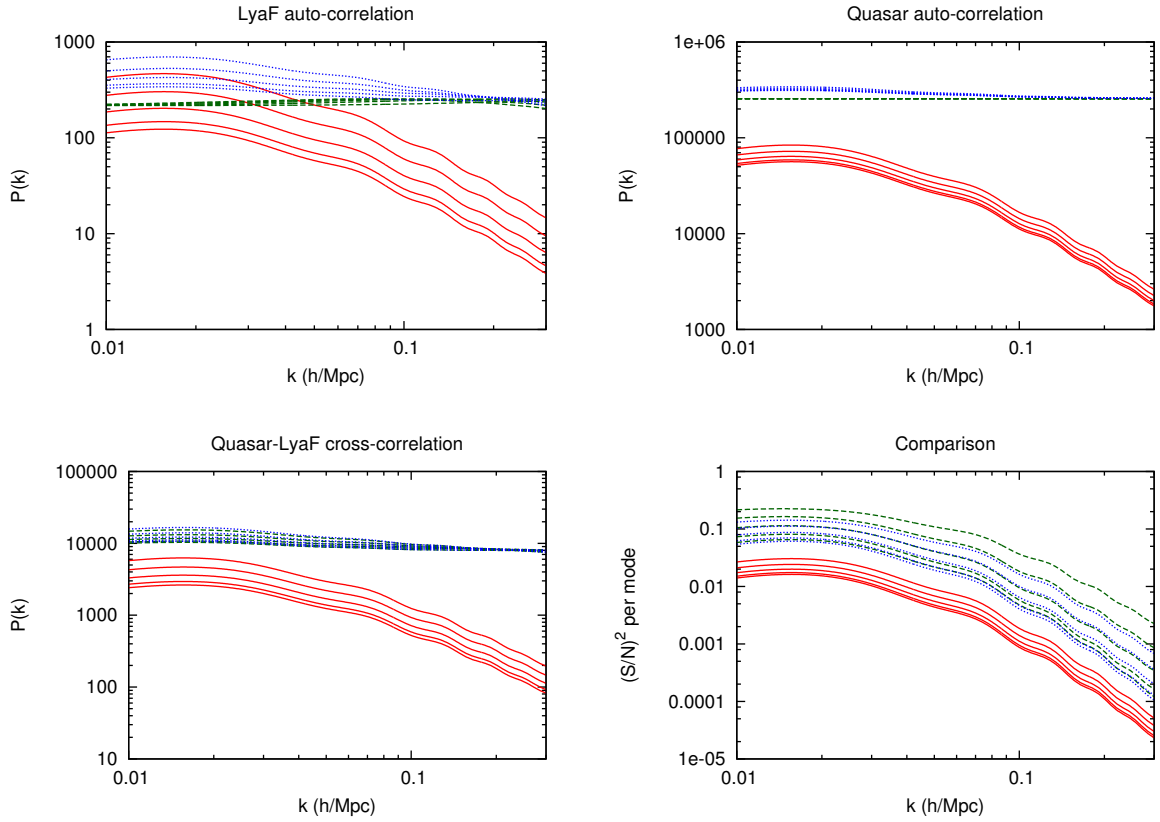

Figure 7: Study of the signal to noise ratio in different analyses: auto-correlation of Lyα (top left), auto-correlation of quasars (top right) and their cross-correlation (bottom left). The red solid lines show the signal, the green dashed lines the "shot noise" level and the dotted blue lines their sum, for different values of μ (increasing from lower to upper lines). The bottom-right panel shows the expected $(S/N)^2$ per mode for the Lyα auto-correlation (dashed green), quasar auto-correlation (solid red) and cross-correlation (dotted blue).

In figure 7 we compare the signal and the different noise contributions for the different analyses: Lyα auto-correlation (top left), quasar auto-correlation (top right) and quasar-Lyα cross-correlation (bottom left). In the bottom-right panel we compare the expected

signal to noise ratio (squared) per mode for the three different analyses, and for different values of μ_k. We can see that the S/N of the quasar-Lyα cross-correlation is much higher than the quasar auto-correlation, and that for transverse modes (lower lines) is as high as the Lyα auto-correlation. It is also clear from the figure that on scales relevant for BAO ($k > 0.05\,h\,\mathrm{Mpc}^{-1}$), we are in the noise-dominated regime, and therefore cosmic variance is at best a secondary contribution to the the error budget.